Effects of Periodic Flow Fluctuations on Magnetic Resonance Flow Images

Yusuf Uludag and Robert L. Powell
Dept. of Chemical Engineering and Materials Science, University of California–Davis, Davis, CA 95616

Michael J. McCarthy
Dept. of Food Science and Technology, University of California–Davis, Davis, CA 95616

DOI 10.1002/aic.10152
Published online in Wiley InterScience (www.interscience.wiley.com).

The effects of periodic velocity fluctuations on magnetic resonance flow images are investigated experimentally and theoretically. In the experiments, laminar pipe flow of water was examined. The flow was driven by a constant pressure head with a superimposed sinusoidal component with the frequency ω_z varied from 0 to 1 Hz, whereas in the simulations ω_z was between 0 to 65 Hz. The velocity profiles obtained from the experimental results compare well with the theoretical calculations. Both theory and experiment show that flow fluctuations produce artifacts in the form of "ghosts" of the primary image, which are spaced at equal intervals in the phase encoding (flow) direction. The distance between ghosts depends on the fluctuation frequency and on the experimentally specified parameters (phase encoding gradient step, repetition time, phase encoding duration, and time difference between phase encoding gradient lobes). The amplitudes of the ghosts depend on amplitude of the flow fluctuation and diminish at frequencies higher than 30 Hz.
 AIChE J, 50: 1662–1671, 2004
Keywords: periodic flow, magnetic resonance flow images, laminar pipe flow, fluid dynamics, rheological properties

Introduction

Characterizing the fluid dynamics and rheological properties of materials during processing is vital to the processing and quality assurance of the product. Considerable effort has been expended in recent years to develop such on-line characterization methods for industrial materials. Common experimental techniques used to measure fluid motion include magnetic resonance imaging, ultrasonic Doppler-echo–based imaging, and laser-Doppler measurements. One goal in the application of these techniques has been to build process sensors based on the tomographic data collected to characterize the material quality, as in the rheological behavior, molecular weight distribution, or degree of uniformity. Successful in-line measurements of fluid properties in actual industrial settings will encounter more challenges than those in carefully controlled laboratory experiments. In the case of magnetic resonance flow imaging the unsteady character of process flows will induce artifacts in the flow images. These unsteady flow–induced artifacts can sufficiently influence the actual magnetic resonance imaging measurements to prevent or limit the estimation of material properties needed for process control and/or quality assurance.

In most applications of magnetic resonance imaging (MRI), the proton spin density is determined as a function of the spatial coordinates. These measurements are represented through variations in image intensity that reflect the local concentration of protons and the effects of spin relaxations, chemical shift, and dipolar and scalar coupling interactions. The signal intensity in the image varies according to the conditions within a volume

Correspondence concerning this article should be addressed to R. L. Powell at rlpowell@ucdavis.edu.

element, or voxel. Variations can also occur as a result of spin motion during magnetic field gradient application. For example, diffusion and flow affect the magnitude and the phase of the magnetic resonance (MR) signal, respectively, and can appear to degrade image quality. Because medical science and technology overwhelm all other uses of MRI, particular attention has been paid to eliminating related artifacts that are associated with physiological movements and with the unsteady nature of blood flow (Duerk and Wendt, 1993). A class of movements of particular interest are those that can be considered as periodic. For example, breathing and cardiac motion cycles occur at periods of approximately 5 and 1 s, respectively. The artifacts generated by such periodic motions appear in the images as repeating ghosts of the principal structures, spaced at regular intervals in the phase-encoding direction. These have been characterized in earlier studies (Frank et al., 1993; Haacke and Patrick, 1986; Wood and Henkelman, 1985).

Effects arising from unsteady flow are critical when MRI is used to produce flow images that provide velocity information (MR flow image) (Izen and Haacke, 1990; Li et al., 1994). Such images show the spin density as a function of a spatial coordinate and the displacement of voxels over a specified elapsed time. In the case of laminar flow, such an image can be easily transformed into the velocity profile. If velocity fluctuations are present, such as those arising from turbulent flow or from the presence of particles in a laminar flow, the quality of the MR flow image—and thus the quantitative data obtained from such images—is adversely affected (Li, 1991; Seymour, 1994). Flow artifacts result mainly from: (1) an increase in signal intensity attributed to a wash-out of partially excited spins that lead to a smaller magnetization component for the successive phase-encoding steps; (2) a decrease in signal intensity attributed to loss of the spins; and (3) an additional phase of the spins caused by their displacement during phase-encoding gradient application (Riek et al., 1993). The size of the first two effects can be directly related to the average residence time of a spin within the imaging volume, and thus to the volumetric flow rate, relative to MRI experimental time scales (repetition and echo times). Additional phase effects depend both on the magnetic field gradient strength and duration in the flow direction and on the volumetric flow rate.

Methods have been developed to minimize or eliminate the influence of periodic motions on MRI data. There are two basic methods: gating of the MR experimental timing to coincide with the fluctuation; or making the image insensitive to a specific type of motion, through proper design of the gradient waveform. In general neither of these techniques will be applicable in all industrial settings. The periodic motions generated by pumps will include both acceleration and higher-order terms. Thus, design of a gradient waveform would need to be matched to the pump at each installation and modified with time as the pump ages and wears. Such an approach also requires sufficient signal evolution time during the experiment and for many industrial fluids the signal decay is very rapid, thereby constraining this approach. Gating of the signal to the motion of a pump may be possible in some instances, although in many operations multiple process streams and multiple pumps would make gating problematic.

Because of its noninvasive and nondestructive characteristics, as well as its applicability to both opaque and transparent media, one application of MR flow imaging has been to study the rheological behavior of fluids (Arola et al., 1999; Callaghan and Xia, 1991; Gibbs et al., 1996; Powell et al., 1994). Here flow fluctuations, resulting from pump action, have been observed to decrease image quality, making their further analysis difficult (Arola et al., 1997, 1998). The effects of pump fluctuations on image quality have been observed to be similar to the effects of movements within the human body, although the frequencies of the periodic motion resulting from pumps range from 0.1 Hz to greater than 100 Hz. In other applications, such as the measurement of turbulent flows or laminar flows of suspensions, a wider range of frequencies is encountered. Taken together, it is clear that to further the use of MRI in new fields, it is crucial to understand the effects of the flow fluctuations on the MR flow images, which is the objective of this work.

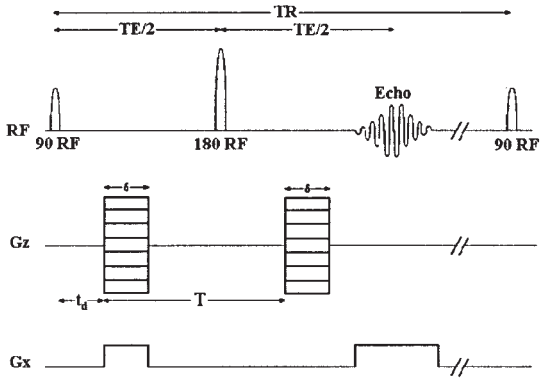

Figure 1. Pulsed-gradient spin echo pulse-sequence used in the experiments and the simulations.

Simulations

A model was developed to predict MR flow imaging data. The method tracks the effects of the flow and the MRI experimental parameters on the phase evolution of an isochromate, which is an ensemble of spins that experience the same flow and MR effects. Assuming the magnetization magnitude of the each isochromate is unity, the real and imaginary components of the signal originating from an isochromate are calculated from the phase of its magnetization. These are then summed separately for all isochromates, to form the corresponding components of the total signal. This is encoded with the spatial and velocity information for each voxel, at a particular data-acquisition time. This procedure is repeated for each data-acquisition point and each phase-encoding step.

The MRI experiment is characterized through the pulse sequence, which specifies the order and timing for the excitations applied to the sample. There are many types of pulse sequences used to encode spatial or velocity information by varying excitation order and timing through the application of different radio frequency (RF) and magnetic field gradient pulses. A standard pulsed-gradient spin-echo pulse sequence, shown in Figure 1, was used in this study. In this pulse sequence spatial encoding is achieved through frequency encoding, whereas phase encoding is applied for velocity. Time parameters include: t_d, the period between 90° RF pulse and the beginning of the first z direction magnetic field gradient; G_z,

lobe; δ, the duration of the G_z lobe; and T, the flow time or time difference between the beginning of G_z lobes. Other timing parameters shown are T_E and T_R, which are the echo and repetition times, respectively.

Simulation development

The model is based on the standard analysis of pulse sequences given by Callaghan (1991). We tailored the analysis to consider unidirectional flow in a tube. The transverse or radial position is frequency encoded, whereas the axial displacement is phase encoded using the gradients G_x and G_z, respectively. The time-domain signal that is acquired can be represented as

$$S(l, q, T) = \int \rho(r)\exp(ilr) \int P(\Delta z, r; T)\exp(iq\Delta z)d\Delta z dr \tag{1}$$

where $l = \gamma G_x t$, $q = \gamma G_z \delta$, and γ is the gyromagnetic ratio of the spins. The angles in the exponential functions in Eq. 1 are the phases of the spins accumulated during a pulse sequence. Spatial and displacement information of the spins is encoded in terms of their phases through l and q, respectively. A Fourier transform with respect to these parameters produces a map of $P(\Delta z, r; T)\rho(r)$ for each radial position, where $P(\Delta z, r; T)$ is the conditional probability density that a spin at position r displaces Δz within the time interval T. Provided that the flow is steady, velocity data can be obtained from the image by dividing Δz by T at each radial position.

In many cases, however, flows are not steady, at least within the time scales of the pulse-sequence parameters. These usually have a range between a few milliseconds and seconds, and in some cases as described above, they can be approximated as periodic. In this study, to simulate flow fluctuation effects, the axial velocity is modeled as a time-averaged part with a superimposed sinusoidal fluctuation

$$V_z(r, t) = U_z(r) + v_z(r)\sin(\omega_z t) \tag{2}$$

where U_z is the time-averaged velocity, and v_z and ω_z are amplitude and frequency of the flow fluctuation, respectively. The precession frequency of the spins is the product of the gyromagnetic ratio and the total magnetic field, also known as the Larmor relation. Thus, in the rotating frame, which has a basic frequency corresponding to the main magnetic field of the medium, the phase of a spin attributed to the applied magnetic field gradient $\mathbf{G}$ is the time integral of the relative frequency, given by

$$\Phi(t) = \int_t \gamma \mathbf{G}(t') \cdot \mathbf{r}(t')dt' \tag{3}$$

where the "$\cdot$" denotes the scalar product.

Considering only the x- and z-directions, the phase of the signal that is emitted by spins at a phase-encoding step, as shown in Figure 1, can be written as

$$\Phi(t_1, \hat{t}) = \gamma \int_{\hat{t}}^{\hat{t}+T_E+t_1} G_x(t')x(t')dt' + \gamma \int_{\hat{t}}^{\hat{t}+T_E+t_1} G_z(t', \hat{t})z(t')dt' \tag{4}$$

where t_1 is the data acquisition time. The time base for t_1 in this analysis is zero at the center of the echo.

The time elapsed between the beginning of the imaging and a phase-encoding step is $\hat{t}_0$. It can be represented as $\hat{t} = nT_R$, where $(N_z/2 - 1) \le n \le N_z/2$, and N_z is the total number of phase-encoding steps. Using the pulse-sequence parameters shown in Figure 1, Eq. 2 for the evaluation of the displacement, and assuming flow is unidirectional, Eq. 4 can be rewritten as

$$\Phi(t_1, \hat{t}) = -\gamma G_x x t_1 + \gamma G_z(\hat{t})\left\{\int_{\hat{t}+t_d}^{\hat{t}+t_d+\delta}\int_{\hat{t}_0}^{t'} [U_z(r) + v_z(r)\sin(\omega_z t'')]dt''dt' - \int_{\hat{t}+t_d+T}^{\hat{t}+t_d+\delta+T}\int_{\hat{t}_0}^{t'} [U_z(r) + v_z(r)\sin(\omega_z t'')]dt''dt'\right\} \tag{5}$$

where $\hat{t}_0$ is the time at which the imaging starts, $\hat{t}_0 = -(N_z/2 - 1)T_R$. Using $\hat{t}_0$ as the lower limit of the displacement integral ensures that the velocity phase difference between successive phase-encoding steps is taken into account. The negative signs in Eq. 5 are ascribed to the effect of the 180° RF pulse. After integration, Eq. 5 becomes

$$\Phi(t_1, \hat{t}) = -\gamma G_x x t_1 - \gamma U_z(r)\delta T G_z(\hat{t}) - \frac{4\gamma v_z(r)G_z(\hat{t})}{\omega_z^2} \times \sin\left(\frac{\delta}{2}\omega_z\right)\sin\left(\frac{T}{2}\omega_z\right)\sin\left[\left(\hat{t} + t_d + \frac{\delta + T}{2}\right)\omega_z\right] \tag{6}$$

Equation 6 shows the relation between the position and velocities, and the phases of the spins that develop as a result of the application of the pulse sequence. Because the MRI signal is dependent on the phases of the spins through $\exp(i\Phi)$, using Eq. 6 we find

$$\exp[i\Phi(t_1, \hat{t})] = \exp(-i\gamma G_x x t_1) \times \exp[-i\gamma U_z(r)\delta T G_z(\hat{t})]\exp\left\{-i\frac{4\gamma v_z(r)G_z(\hat{t})}{\omega_z^2}\sin\left(\frac{\delta}{2}\omega_z\right) \times \sin\left(\frac{T}{2}\omega_z\right)\sin\left[\left(\hat{t} + t_d + \frac{\delta + T}{2}\right)\omega_z\right]\right\} \tag{7}$$

In an actual experiment, the gradient G_z is incremented by ΔG_z for each phase-encoding step. Then, $\hat{t}$ can be expressed in terms of G_z through $\hat{t} = G_z T_R/\Delta G_z$. By using the identity (Wood and Henkelman, 1985)

$$\exp(iA\sin B) = \sum_{k=-\infty}^{\infty} \exp(ikB) J_k(A) \tag{8}$$

Eq. 7 becomes

$$\exp[i\Phi(t_1, G_z)] = \exp(-i\gamma G_x x t_1)\exp[-i\gamma U_z(r)\delta T G_z] \times \sum_{k=-\infty}^{\infty} \exp\left[ik\left(\frac{T_R G_z}{\Delta G_z} + t_d + \frac{\delta + T}{2}\right)\omega_z\right] J_k(KG_z) \tag{9}$$

where J_k is the kth order Bessel function of the first kind and K is given by

$$K = -\frac{4\gamma v_z(r)}{\omega_z^2}\sin\left(\frac{\delta}{2}\omega_z\right)\sin\left(\frac{T}{2}\omega_z\right) \tag{10}$$

Assuming that the magnetization within the sample is unity, so that $\rho(r)$ is constant, Eq. 9 can then be considered as the MRI signal at a certain data-acquisition and phase-encoding step as a function of position and velocity. The total MRI signal at that particular time in the experiment is the summation of the signals corresponding to all positions and velocities in the system, weighted by their respective conditional probabilities. Therefore, neglecting the effects of the discrete nature of MRI, from Eq. 1 it follows that a two-dimensional (2-D) Fourier transform of Eq. 9 with respect to t and G_z yields $P(\Delta z, r; T)$, given by

$$P(\Delta z, r, T) = AF\langle F\{\exp[i\Phi(t_1, G_z)]\}\rangle = A\left[\delta\left(f_x + \frac{\gamma}{2\pi}G_x x\right)\delta\left(f_z + \frac{\gamma\delta T}{2\pi}U_z(r)\right)\right] * \left\{\sum_{k=-\infty}^{\infty}\exp\left[ik\left(t_d + \frac{\delta + T}{2}\right)\omega_z\right] F[J_k(KG_z)] * \delta\left(f_z - \frac{kT_R\omega_z}{2\pi\Delta G_z}\right)\right\} \tag{11}$$

where f_x and f_z are the independent variables in the frequency domain with the units of Hz and m/T, respectively; A is a constant that is proportional to spin density; and $\delta(x)$ is the Dirac delta function.

In this study the flow medium is water, with uniform spin density throughout the imaging volume, leading Eq. 11 to govern the intensity distribution on the two-dimensional frequency domain that is the resultant MR flow image. For a particular point x_0 within the flow, $P(\Delta z, r; T)$ can also be expressed in terms of spatial and velocity coordinates x and u_z as

$$P(\Delta z, r, T) = A\{\delta(x + x_0)\delta[u_z + U_z(x_0)]\} * \left\{\sum_{k=-\infty}^{\infty}\exp\left[ik\left(t_d + \frac{\delta + T}{2}\right)\omega_z\right] F[J_k(KG_z)]\delta * \left(u_z - \frac{kT_R}{\gamma\delta T\Delta G_z}\omega_z\right)\right\} \tag{12}$$

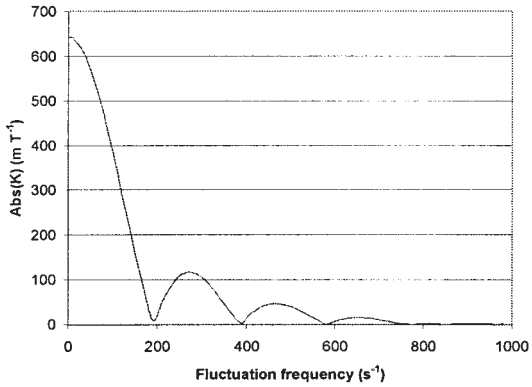

Figure 2. $|K|$ values with respect to flow fluctuation frequency ω_z at typical MRI experimental parameters and at an average velocity of 0.1 m s^{-1}.

Equation 12 indicates that in addition to the average velocity profile, artifacts in the form of "ghosts" of the profile appear in the image. They are placed at equal intervals of $T_R\omega_z/(\gamma\delta T\Delta G_z)$ and with amplitudes dependent on the pulse-sequence and flow velocity through Fourier transform of $J_k(KG_z)$, which is given by (Abramowitz and Stegun, 1964)

$$F[J_k(KG_z)] = \begin{cases} \dfrac{2(-i)^k T_k\left(\dfrac{\gamma\delta T u_z}{K}\right)}{[K^2 - (\gamma\delta T u_z)^2]^{1/2}} & \left|\dfrac{\gamma\delta T u_z}{K}\right| < 1 \\ 0 & \left|\dfrac{\gamma\delta T u_z}{K}\right| > 1 \end{cases} \tag{13}$$

where T_k is Chebyshev polynomial of kth order. From the last delta function in Eq. 12, the positions of the ghosts on the velocity axis are at $u_z = kT_R\omega_z/(\gamma\delta T\Delta G_z)$. According to Eq. 13, among the ghosts of different index k, only those up to values of k that satisfy the criterion $|\gamma\delta T u_z/K| < 1$, which can also be expressed as $|kT_R\omega_z/(K\Delta G_z)| < 1$, appear in the image. Above that index k, their u_z positions become large enough for their intensity to vanish. The criterion in Eq. 13 specifies that, for a ghost attributed to the fluctuating component of the flow to appear, its MR phase should be comparable to or greater than the phase associated with an average velocity corresponding to the ghost position u_z. The function $|K|$ has the form of the square of a sinc function $[\sin(\omega_z)/\omega_z]$, and is plotted in Figure 2. In the figure typical pulse-sequence parameters are used along with a fluctuation amplitude of 0.01 m/s, a typical value at the pipe center where $U_z \approx 0.1$ m/s. One can expect ghosts to appear in images up to higher k indexes with the intervals between them decreasing as the fluctuation frequency decreases. At sufficiently low frequencies and for a fixed-oscillation displacement amplitude, the ghosts become small and disappear at $\omega_z = 0$.

For the pulse sequence used, we can write the velocity resolution as $2\pi/(N_z\gamma\delta T\Delta G_z)$. Also, by using the expression for the ghost separation given in Eq. 12, successive ghosts cannot be distinguished if $\omega_z < 2\pi/(N_z T_R)$. Because of the small intervals between the ghosts of low-frequency fluctuations, it requires higher k numbers to appear on a particular u_z position compared with higher-frequency fluctuations. The Chebyshev

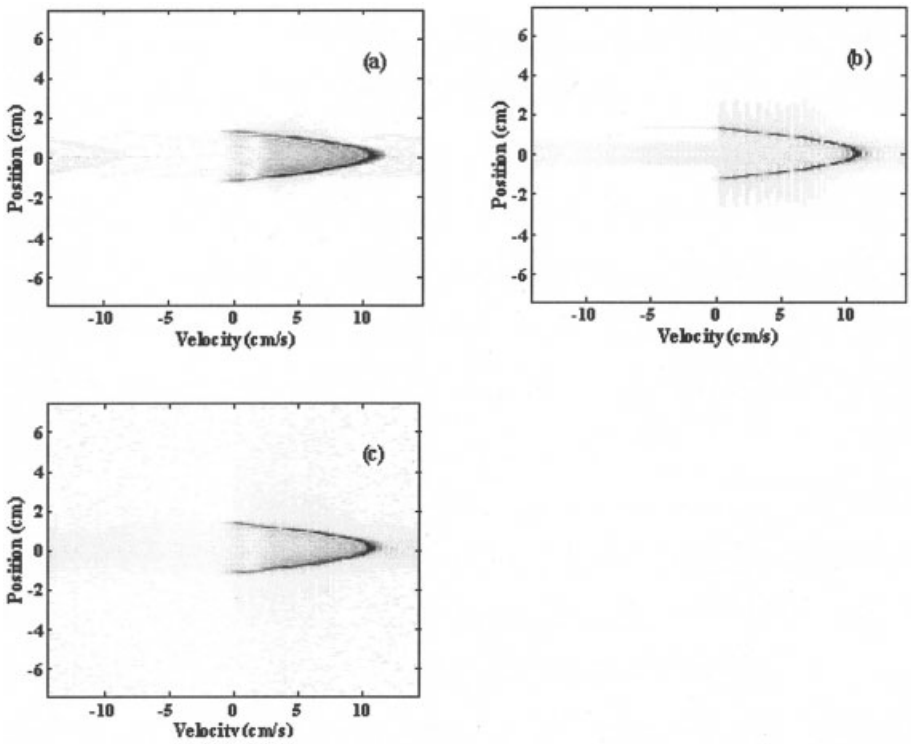

Figure 3. Experimental (a) and simulation (b) results of MRI flow imaging without flow fluctuations at the same experimental parameters; Figure (c) is obtained by superimposing (a) and (b).

polynomials do not tend to diminish at high indexes, leading to having appreciable ghost intensities as long as they satisfy the criterion. In an earlier study (Wood and Henkelman, 1985), it was reported that the intensities of the ghosts with higher indexes tend to decrease and that behavior could be captured by the convolution terms coming from discrete analytical equations. In this study, the results of the simulations at very low frequencies reveal that for a fixed velocity amplitude velocity images consist of the average velocity profile and ghosts forming a continuous shadow filling the entire velocity field and the pipe in the velocity and spatial dimensions, respectively, whereas at a fixed-displacement amplitude, the ghosts disappear. At zero frequency, $|K|$ is a maximum. Normally higher $|K|$ values permit higher k indices or a larger number of ghosts with nonzero intensity. At this particular frequency, however, the ghost shifting becomes zero and from Eq. 12 it follows that no velocity artifacts appear on the image other than at the point corresponding to the average velocity value for a given x position. In other words, all ghosts have the same position as the average velocity on the velocity axis, and thus the image becomes free of the artifacts. According to Eq. 13, there will be intensity contributions to the velocity image at the maximum value of $|K|$. The characteristics of the ghosts are investigated in detail in the Results and Discussion section.

In the absence of the flow fluctuation, the convolution terms disappear and Eq. 11 reduces to

$$P(\Delta z,\, r,\, T) = A\,\delta\left(f_x + \frac{\gamma}{2\pi}\, G_x x\right)\delta\left[f_z + \frac{\gamma \delta T}{2\pi}\, U_z(r)\right] \quad (14)$$

Equation 14 provides the image intensity at each radial position x and the associated velocity through the delta functions for a steady laminar flow, yielding a 2-D projection of the velocity profile.

Simulation implementation

The results of the previous section were implemented in a computer model to simulate the MR flow image by keeping track of the phases of isochromates using Eq. 6. The output of the simulation was processed using MATLAB software to obtain the flow images. The values of the pulse-sequence and flow parameters were identical to those used in the experiments. Special attention was paid to choosing the number of isochromates in the simulated volume. Ideally, a very large number of isochromates would be better in terms of capturing the spin responses. On the other hand, as the number of isochromates increases, the CPU time and memory requirements increase linearly; therefore a reasonable number should be selected. The minimum is given by the Shannon theorem (Bittoun et al., 1984), which states that the frequency difference between the successive isochromates must be smaller than half of the reciprocal of the data acquisition time. In other words there should be more than two isochromates per voxel. In this study the typical G_x value was 8×10^{-3} Tesla (T)/m, corresponding roughly to 3.4×10^5 Hz/m. The data-acquisition period was approximately 5×10^{-3} s, which resulted in a number of isochromates per frequency-encoded length as 3.4×10^3 m^{-1}. To ensure proper sampling of the time domain signal, the number of isochromates used in this study was about

twice the minimum number required. The isochromates were distributed in equal intervals in the x-direction. In the axial direction the phase of the signal depends only on the velocity but not the axial position of the spins. Because the main task in the simulation is tracking phase changes of each isochromate, using one isochromate at a certain spatial position was sufficient to encode the velocity provided that flow is uniform along the axial direction.

For the sake of simplicity, the spin–lattice (T_1) and spin–spin (T_2) relaxations were not considered in the simulations. Therefore the magnetization magnitudes of the isochromates, which were assumed to be unity, remained unchanged throughout the simulation. Neglecting the relaxation terms can be considered reasonable, given that $T_1 < T_R$ and $T_E < T_2$ for tap water. The signal decay between RF pulse excitation and data acquisition or T_E is negligible.

The displacements of the isochromates were calculated by assuming a parabolic profile for the average velocity. Although the analytical expression for the velocity profile of a fluid in tubular flow under a periodic time-dependent pressure gradient is more complicated, it can be approximated as parabolic, provided that the amplitude of the oscillation is small compared to the average velocity (Leal, 1992). The amplitudes of the fluctuation term, $v_z(r)$, were represented as a fraction of the average velocity at each point. In this study that fraction was 0.1, sufficiently small for the parabolic profile assumption.

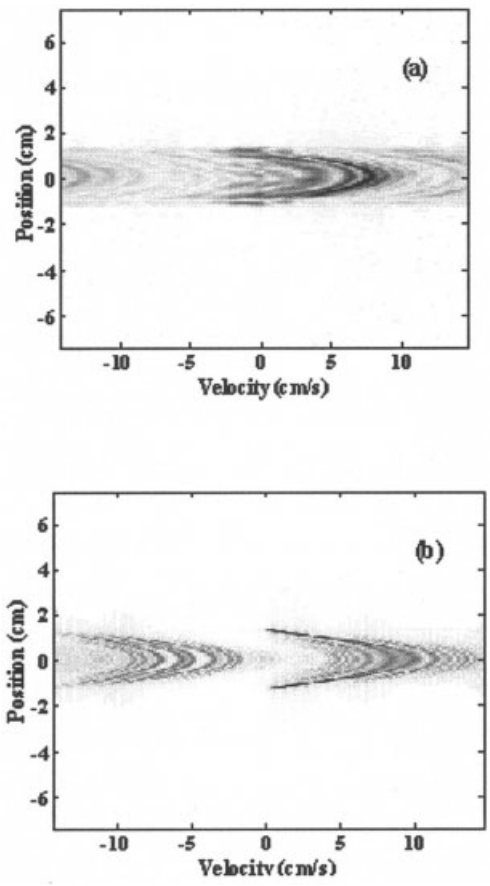

Figure 4. Experimental (a) and simulation (b) results of MRI with flow fluctuation frequency of 0.64 Hz.

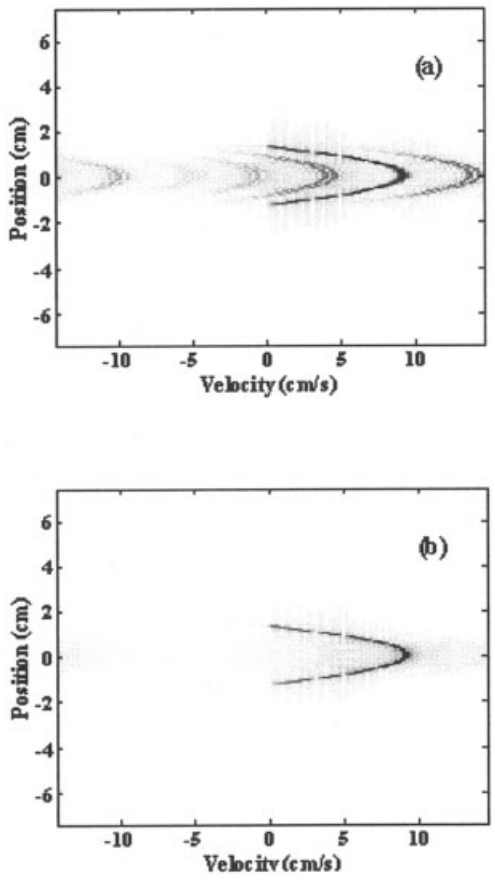

Figure 5. Simulation results at the fluctuation frequencies of 20.5 Hz (a) and 64.9 Hz (b).

Experimental

Magnetic resonance imaging

The MRI system consists of a General Electric CS-II (General Electric Medical Systems, Fremont, CA)/TecMag Libra spectrometer (TecMag, Houston, TX), connected to a 0.6-T Oxford superconducting magnet with a horizontal bore 0.33 m in diameter. The orthogonal magnetic field gradients G_x, G_y, and G_z are driven by an Oxford-2339 water-cooled gradient power amplifier. The diameter and length of the homemade Alderman–Grant-type (Alderman and Grant, 1979) radio-frequency coil are 6×10^{-2} and 11×10^{-2} m, respectively. Similar to the simulations, spatial and velocity encoding are carried out through frequency and phase encoding, respectively. The number of phase-encoding steps was 64, whereas the number of scans for each phase encoding step was 1. Typical values of the pulse-sequence parameters used in the experiments and simulations, G_x, ΔG_z, δ, T, T_E, and T_R, were 0.8×10^{-2} T/m, 0.3×10^{-3} T/m, 7.4×10^{-3} s, 32.5×10^{-3} s, 59.5×10^{-3} s, and 2.3 s, respectively.

Flow loop

The flow system consists of transparent plastic tubing with 2.54×10^{-2} m inner diameter, a static mixer, an in-line flow meter, two plastic tanks, and a variable-speed positive-displacement pump (SPS-20, Sine Pump, Orange, MA). The

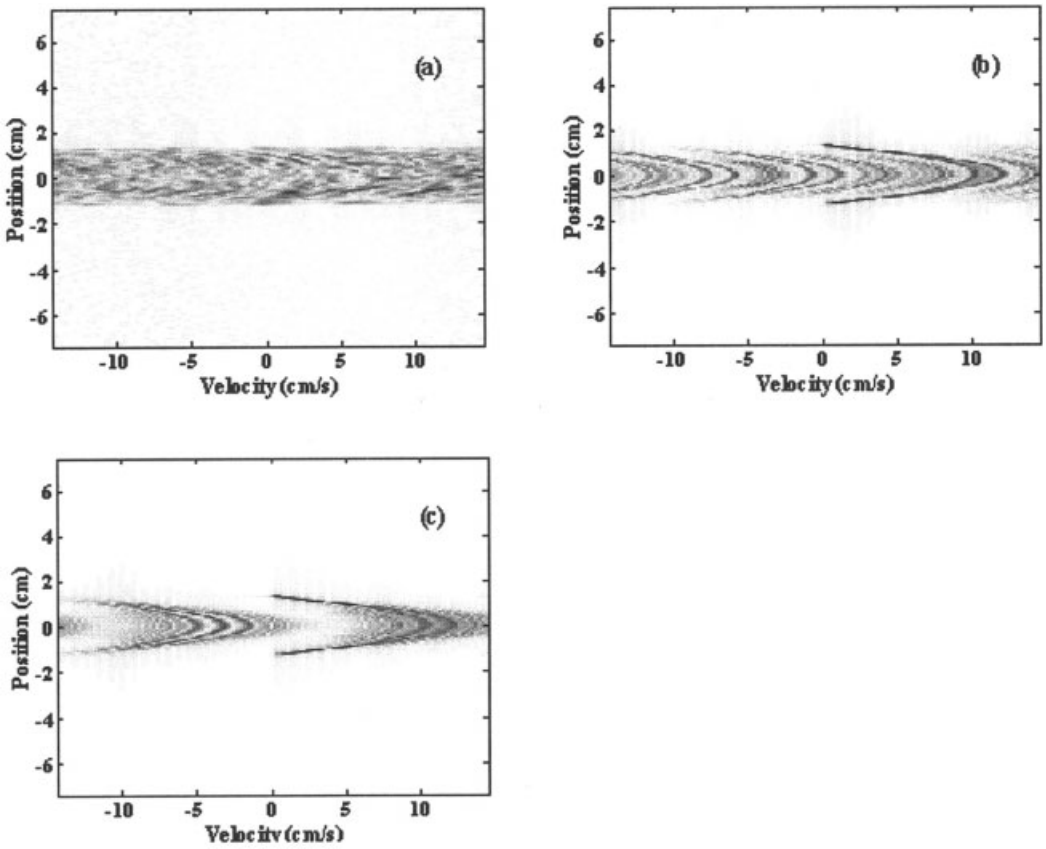

Figure 6. Experimental (a) and simulation (b) results with flow fluctuation frequency of 1.03 Hz.

Even a slight change in the frequency resulted in improved image quality as shown in (c), obtained by simulation at 1.1 Hz.

straight tubing upstream of the magnet bore is 4.5 m in length, which is sufficient to ensure fully developed flow (L/D $\approx$ 175). A constant water head is maintained by pumping tap water from the lower tank to the upper one. Both the overflow from the upper tank and the return flow from experimental section running through the magnet are received in the lower tank. The constant head allowed operation at a steady average flow rate. The flow fluctuation is introduced by connecting the pump outlet stream, which has periodic fluctuations, to the line that passes through the magnet. The frequency and amplitude of the fluctuations are regulated by changing pump speed and by partially opening and closing the valves on the connection between the two lines. The maximum speed at which the pump can be operated is 100 rpm, which corresponds to approximately 1.5 Hz.

Result and Discussion

Figure 3 depicts experimental and simulation images for steady laminar flow of water in a pipe at a Reynolds number of 1520. In the simulation all the flow and MR parameters were identical to those used in the experiment. In this and all subsequent figures the velocities are represented along the horizontal axis and the radial positions along the vertical axis. These figures are obtained using a 2-D Fourier transform of the data acquired in the experiments and generated in the simulations (see Eq. 12). They show the probability of finding spins or isochromates at a particular location and velocity. Dark regions imply that the probability of finding spins at the corresponding location and velocity is higher than that compared to the light regions. For the experimental data, the dark regions represent the projection of the velocity profile, $U_z(r)$, onto a 2-D planar surface. This results in the nonzero signal amplitude interior to the ridge, which is attributed to the projection operation of the paraboloid surface representing the velocity profile in a tube onto a plane. The simulations can be considered as flow between two parallel plates. The projection of this geometry, therefore, yields a sharp velocity image without any dark region inside the ridge, as shown in Figure 3b. Other effects that may result in the observed differences between the two images include magnetic field inhomogeneities and eddy currents that decrease the experimental image quality. Further, the rectangular gradient waveforms assumed in the simulations ignore possible effects of additional phase accumulation of the spins because of the finite rise and fall times of the gradients in the experiments. Despite some differences between the experimental and simulation images, it can be concluded that they compare well with each other. This is clearly seen when the two images are superimposed, as shown in Figure 3c.

We start the analysis of the flow images with a superimposed fluctuation by inferring their appearance at very high and very low values of the flow fluctuation frequency. At very low frequencies, K attains a maximum as shown in Figure 2. Because of the constraint given in Eq. 13, $|\gamma\delta T u_z/K| < 1$, the ghosts up to a large value of index k survive. On the other hand,

the position shifts of the ghosts become very small. Therefore, the resultant image consists of many ghosts with very small separation. This is seen in Figure 4, which shows experimental and simulation results for a fluctuation frequency of 0.64 Hz. The ghosts in the simulations are introduced by including the phase of the spins developed because of the fluctuating part of the flow and it is given by the last term of Eq. 6. These results compare well with each other in terms of capturing the fluctuation effects. Besides a slightly dark ridge indicating the mean velocity profile, the ghosts appearing at equal intervals, as implied by Eq. 12, are the main features of the images. The amplitudes of the ghosts are determined by the flow and pulse-sequence parameters through the Fourier transform of $J_k(KG_z)$ given by Eq. 13.

Increasing the value of the fluctuation frequency results in smaller $|K|$ values, which become almost zero after obtaining local maxima, as seen in Figure 2. Then, even for the ghosts of very small index k, the criterion $|\gamma\delta Tu_z/K| > 1$ holds, implying that there are no effects of the flow fluctuation on the image. Also, because $J_k(0) = 0$ for $k \geq 1$ the only ghost that remains is for $k = 0$, for which there is no position shift. The simulation results at the two high frequencies, 20.5 and 64.9 Hz, are shown in Figure 5. Some ghosts persist at the lower frequency, although they completely disappear at the higher frequency, and the image becomes identical to the one with no fluctuations, as predicted by Eq. 12. $|K|$ has its first local minimum at the frequency 30 Hz. Above that frequency $|K|$ never becomes significantly larger than the $|K|$ value at 64.9 Hz. Therefore, we can conclude that operating at flow fluctuations above 30 Hz results in sufficiently small $|K|$ values for no flow artifacts to appear in the images.

The effects of the intermediate flow fluctuation frequencies, on the order of 1 Hz, are quite complex. While keeping the other parameters constant, operating at different frequencies in this range makes the ghost effects strong or weak without a particular trend because of the complex nature of the functions involved. From Figure 2, it is apparent that near $\omega_z = 1$ Hz $|K|$ is close to its maximum. Therefore, ghosts up to large k indexes can be expected to have appreciable amplitude. High index values coupled with moderate ghost shifting can lead to the ghost positions on the velocity axis larger than half of the maximum velocity that can be encoded, giving rise to the wraparound of the velocity image, which is also known as *aliasing*. At some particular frequencies, the aliased ghosts completely dominate the image such as for the case depicted in Figure 6, which shows the images obtained by experiments and simulations at the fluctuation frequency of 1.03 Hz. Even a slight deviation from that frequency value is observed to improve the flow image quality appreciably with distinguishable flow patterns, as seen in Figure 6c, obtained using a frequency of 1.1 Hz.

Equation 12 indicates that the pulse-sequence parameters phase-encoding gradient step ΔG_z, phase-encoding duration δ, and flow time T have the same effects on the ghost positions; that is, decreasing any of them will result in an increase in ghost separation by the same amount. The field of view in the flow direction (that is, the total range of velocity) is another property of the images that is also inversely proportional to those parameters. Therefore, the relative positions of the ghosts appear the same when any of the parameters above are changed. Halving the values of δ and T, used in the calculation

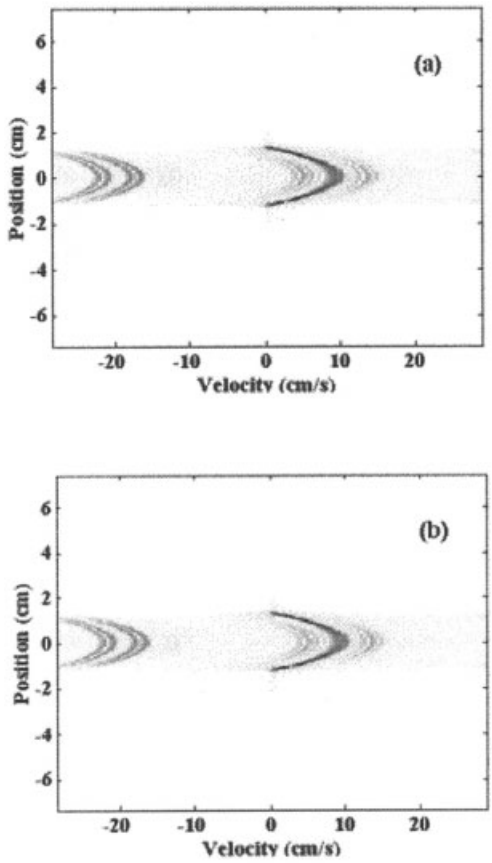

Figure 7. Simulation results at $\delta = 3.7 \times 10^{-3}$ s (a) and at Tesla (T) = 16.27×10^{-3} s (b), corresponding to the half value of the values used in Figure 4b.

shown in Figure 4b, obtains simulation results shown in Figures 7a and b, respectively. All other pulse-sequence and flow parameters are the same for both figures. They show that decreasing the values of δ or T causes the ghost separation and velocity field of view to increase by the same proportion. Also, δ and T play a role in ghost amplitudes through Eq. 13. Because δ and T are typically on the order of milliseconds, the arguments of the Eq. 10 will be small for moderate fluctuation frequencies, and the dependency of K on δ and T can be approximated as linear instead of sinusoidal; thus, effects of δ and T on the resultant image can be considered as identical. The larger they become, the higher the index k becomes, which increases the number of ghosts with appreciable amplitudes.

The parameters ΔG_z and repetition time T_R have opposite effects on the ghost separations and amplitudes, as seen in Figure 8. Both simulated images in Figure 8 were obtained using the same parameters as those in Figure 4b, except that ΔG_z was changed in Figure 8a and T_R in Figure 8b. As implied by Eq. 12, decreasing the ΔG_z yields wider ghost separation, whereas increasing T_R gives a similar result. In terms of velocity field of view and ghost separation, ΔG_z has the same effects as δ and T, as expected. That can be seen when Figure 8a is compared with Figures 7a and 7b. The criteria for the ghosts to have an appreciable intensity can be expressed in a different way by substituting the terms in the last delta function

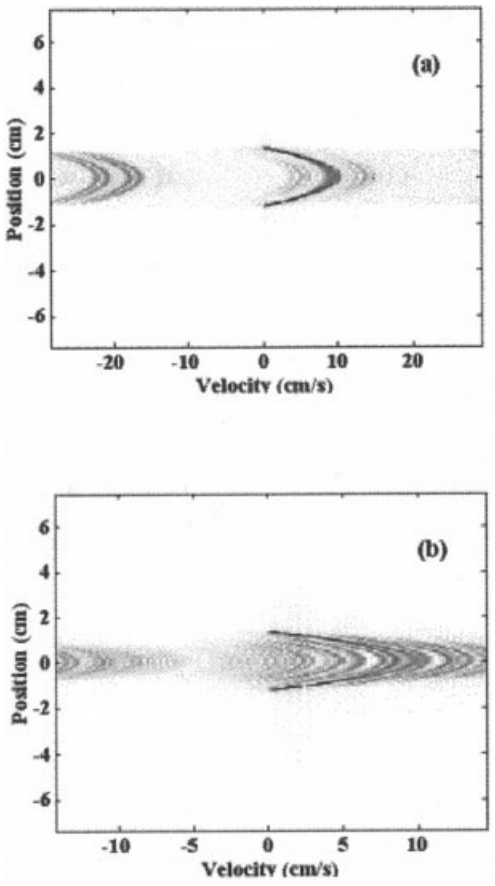

Figure 8. Simulation results at $\Delta G_z = 0.15 \times 10^{-3}$ T m^{-1} (a) and at TR = 4.6 s (b), corresponding to the half and twice the values used in Figure 4b, respectively.

in Eq. 12 for the ghost positions on the velocity axis u_z, in Eq. 13, yielding $kT_R\omega_z/(K\Delta G_z) < 1$. It can be concluded that ΔG_z has the same effect on the ghost intensities as K. Therefore we can expect that the number of ghosts has the same dependency on the parameters ΔG_z, δ, and T within the typical range of the parameters, as shown in Figures 7 and 8a. On the other hand, T_R has an opposite effect on the ghost intensities compared with that of ΔG_z. The net result of increasing T_R is an image with a smaller number ghosts having larger separations, as shown in Figure 8b. The other difference between Figures 8a and b is in their velocity axis scales, given that changing T_R has no effect on the velocity field of view, as seen in Figures 4b and 8b.

Another flow parameter that affects the flow images is the amplitude of the fluctuation, v_z. Equation 12 predicts that v_z plays a role in the intensity of the ghosts through the Bessel function. To test this, simulations were performed at the fluctuation amplitudes of 10 and 50% of the fluctuation used in the simulation shown in Figure 4. The results are depicted in Figure 9, which shows that the ghost intensities increase as v_z increases, whereas their positions remain unchanged. Another effect of ghost amplitude is that more ghosts appear in the center region of the pipe. The main reason for that is the higher flow fluctuation amplitudes in the regions close to the pipe center, compared with those close to the pipe wall. Fluctuation amplitudes at each radial position were specified by taking 10% of the time-averaged velocity at the corresponding radial positions.

Conclusions

For MR flow images, periodic flow fluctuations have strong effects on the artifacts that appear as repeating ghosts in the phase-encoding direction. The frequencies of the fluctuations determine the separation distance and the amplitudes of the ghosts. In comparison to other flow and MRI pulse-sequence parameters, the flow fluctuation amplitude is at least of equal importance in governing the ghosts. As the fluctuation frequency increases, the ghosts are less apparent. Therefore at frequencies above 30 Hz, for typical experimental parameters used in MR flow imaging, periodic flow fluctuations will not significantly influence the measured velocity profile. At moderate frequencies, there is no particular trend in ghost formation with respect to fluctuation frequency because of the complex nature of the interaction. The effects of the other pulse-sequence parameters, such as phase-encoding duration, flow time, and phase-encoding gradient step, have the same effects on the ghosts and resultant MR image in terms of the distance between ghosts and velocity field of view, whereas the ghost

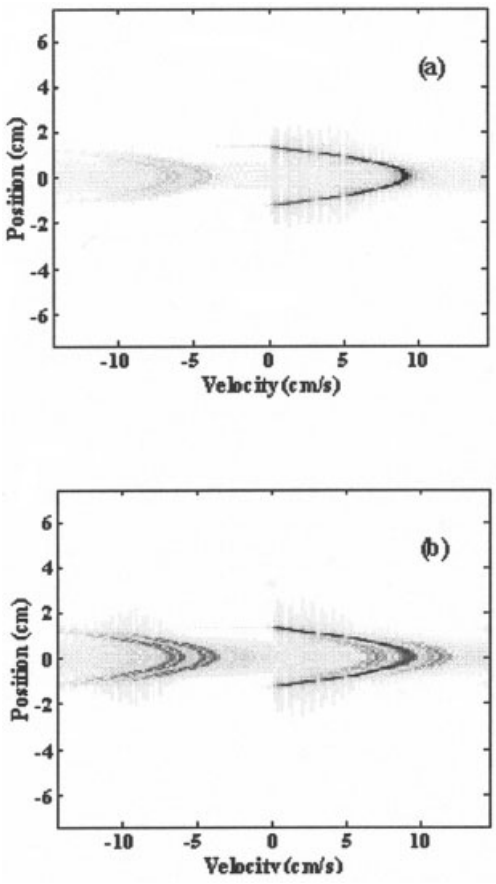

Figure 9. Simulation results at the fluctuation frequency of 0.64 Hz and mean flow to fluctuation amplitudes ratios of 0.01 (a) and 0.05 (b), corresponding to 10 and 50% of the fluctuation amplitude used in Figure 4b, respectively.

separation is directly proportional to the repetition time as opposed to the other pulse-sequence parameters. The amplitude of the flow fluctuations influences only the intensities of the ghosts. Finally, this work shows that in practical applications of MRI to industrial problems, artifacts that are likely to be encountered can be estimated a priori and appropriate corrections can be made. This potentially allows for a wider range of applications as well as lower cost implementation of the technology.

Acknowledgments

This study is supported by the Department of Energy through Grant DE-FG07-96ER14727 and the Center for Process Analytical Chemistry, University of Washington.

Literature Cited

Abramowitz, M., and I. A. Stegun, eds. *Handbook of Mathematical Functions, with Formulas, Graphs, and Mathematical Tables*, U.S. National Bureau of Standards, Washington, DC, p. 486 (1964).

Alderman, D. W., and D. M. Grant, "Efficient Decoupler Coil Design Which Reduces Heating in Conductive Samples in Superconducting Spectrometers," *J. Magn. Reson.*, **36**, 447 (1979).

Arola, D. F., G. A. Barrall, R. L. Powell, K. L. McCarthy, and M. J. McCarthy, "Use of Nuclear Magnetic Resonance Imaging as a Viscometer for Process Monitoring," *Chem. Eng. Sci.*, **52**, 2049 (1997).

Arola, D. F., R. L. Powell, G. A. Barrall, and M. J. McCarthy, "A Simplified Method for Accuracy Estimation of Nuclear Magnetic Resonant Imaging," *Rev. Sci. Instrum.*, **69**, 3300 (1998).

Arola, D. F., R. L. Powell, G. A. Barrall, and M. J. McCarthy, "Pointwise Observations for Rheological Characterization Using Nuclear Magnetic Resonance Imaging," *J. Rheol.*, **43**, 9 (1999).

Bittoun, J., J. Taquin, and M. Sauzade, "A Computer Algorithm for the Simulation of any Nuclear Magnetic Resonance (NMR) Imaging Method," *Magn. Reson. Imaging*, **2**, 113 (1984).

Callaghan, P. T., *Principles of Nuclear Magnetic Resonance Microscopy*, Oxford University Press, New York, p. 338 (1991).

Callaghan, P. T., and Y. Xia, "Velocity and Diffusion Imaging in Dynamic NMR Microscopy," *J. Magn. Reson.*, **91**, 326 (1991).

Duerk, J. L., and R. E. Wendt III, *Magnetic Resonance Angiography: Concepts and Applications*, edited by E. J. Potchen, et al., eds., Mosby-Year Book, St. Louis, MO (1993).

Frank, L.R., R. B. Buxton, and C. W. Kerber, "Pulsatile Flow Artifacts in 3D Magnetic Resonance Imaging," *Magn. Reson. Med.*, **30**, 296 (1993).

Gibbs, S. J., K. L. James, and L. D. Hall, "Rheometry and Detection of Apparent Wall Slip for Poiseuille Flow of Polymer Solutions and Particulate Dispersions by Nuclear Magnetic Resonance Velocimetry," *J. Rheol.*, **40**, 425 (1996).

Haacke, E. M., and J. L. Patrick, "Reducing Motion Artifacts in Two-Dimensional Fourier Transform Imaging," *Magn. Reson. Imaging*, **4**, 359 (1986).

Izen, S. H., and E. M. Haacke, "Measuring Nonconstant Flow in Magnetic Resonance Imaging," *IEEE Trans. Med. Imaging*, **9**, 450 (1990).

Leal, G. L., *Laminar Flow and Convective Transport Processes: Scaling Principles and Asymptotic Analysis*, Butterworth–Heinemann, Boston, MA, p. 105 (1992).

Li, T. Q., "Interaction between Water and Cellulose Fibers: Application of NMR Techniques," PhD Thesis, Royal Institute of Technology, Stockholm, Sweden (1991).

Li, T. Q., J. D. Seymour, R. L. Powell, K. L. McCarthy, L. Odberg, and M. J. McCarthy, "Turbulent Pipe- Flow Studied by Time-Averaged NMR Imaging-Measurements of Velocity Profile and Turbulent Intensity," *Magn. Reson. Imaging*, **12**, 923 (1994).

Powell, R. L., J. E. Maneval, J. D. Seymour, K. L. McCarthy, and M. J. McCarthy, "Note: Nuclear Magnetic Resonance Imaging for Viscosity Measurements," *J. Rheol.*, **38**, 1465 (1994).

Riek, J. K., S. M. Totterman, A. M. Tekalp, W. E. Smith, and E. Kwok, "Flow Compensation in MRI Using a Phase-Corrected Real Reconstruction," *Magn. Reson. Med.*, **30**, 724 (1993).

Seymour, J. D., "MRI Investigation of Fluid and Suspensions Mechanics," PhD Thesis, University of California, Davis (1994).

Wood, M. L., and R. M. Henkelman, "MR Image Artifacts from Periodic Motion," *Med. Phys.*, **12**, 143 (1985).

Manuscript received Sep. 11, 2002, and revision received Oct. 7, 2003.